

Cross-field chaotic transport of electrons by $\mathbf{E} \times \mathbf{B}$ electron drift instability in Hall thruster

D. Mandal,^{1,2} Y. Elskens,¹ N. Lemoine,³ and F. Doveil¹

¹*Aix-Marseille Université, CNRS, UMR 7345-PIIM Laboratory, Marseille, France*

²*Indo-French Centre for the Promotion of Advanced Research-CEFIPRA, New Delhi, India*

³*Université de Lorraine, Institut Jean Lamour, UMR-7198, CNRS, France*

A model calculation is presented to characterize the anomalous cross-field transport of electrons in a Hall thruster geometry. The anomalous nature of the transport is attributed to the chaotic dynamics of the electrons arising from their interaction with fluctuating unstable electrostatic fields of the electron cyclotron drift instability that is endemic in these devices. Electrons gain energy from these background waves leading to a significant increase in their temperature along the perpendicular direction $T_{\perp}/T_{\parallel} \sim 4$ and an enhanced cross-field electron transport along the thruster axial direction. It is shown that the wave-particle interaction induces a mean velocity of the electrons along the axial direction, which is of the same order of magnitude as seen in experimental observations.

Keywords : ExB drift instability, Hall thruster, Chaos

PACS :

52.20.Dq Particle orbits

52.25.Fi Transport properties

52.75.Di Ion and plasma propulsion

I. INTRODUCTION

Hall thrusters [1] are gridless ion sources that are frequently used as space propulsion devices in geostationary satellites and long range missions such as Earth to Moon missions. They have been the subject of many past studies [2–8]. A salient feature observed in such studies is the presence of a strong cross-field anomalous electron transport along the axial direction of the thruster. This has been consistently observed both in model numerical simulations [5–7] as well as in laboratory experiments [2–4], and a detailed understanding of this anomalous transport process is still lacking. Since the efficiency of the thruster decreases with an increase in the anomalous electron transport [4], it is important to gain some understanding of the underlying mechanism driving such a transport.

Our present work is motivated by a desire to throw some light on this process, and we attempt to do so by analyzing the characteristics of this transport and developing a physics model to describe the origin of the transport. Since the ionization efficiency in the thruster chamber is more than 90%, the density of neutral atoms is so low that electron collisions cannot explain the high electron flux observed experimentally. Indeed, the electron transport coefficients are 100 times larger than those given by the collisional transport model [9]. Since the collisional transport fails to explain the observed cross-field electron transport after the channel exit, other explanations have been proposed in the past. Among them the non-collisional transport due to the interaction of electrons with the electric fields of the numerous electrostatic instabilities that can occur is an attractive candidate. Indeed, 2D (azimuthal and axial) PIC simulations [5] show that turbulence alone (without any wall conduc-

tivity that could not be modeled in this simulation) is able to drive a high enough electron transport to explain anomalous transport. The dominant instability seen in those simulations was also observed experimentally [3] and identified theoretically as the $\mathbf{E} \times \mathbf{B}$ electron drift instability [10].

The $\mathbf{E} \times \mathbf{B}$ electron drift instability, also called the electron cyclotron drift instability or beam cyclotron instability [11], is observed in a magnetized plasma under conditions when the ion motion is hardly modified by the magnetic field whereas the electrons experience a strong drift, resulting in a huge velocity difference between electrons and ions. The frequency of this instability is much lower than the electron cyclotron frequency ($\omega \ll \omega_c$). Therefore, the resonance condition with the cyclotron harmonics, $\omega - k_{\parallel}v_{\parallel} = n\omega_c$ is not satisfied. The frequency is of the order of the ion acoustic wave frequency.

The mechanism of the instability is the following. Bernstein waves (whose frequencies are multiples of the electron cyclotron frequency) are Doppler-shifted towards low frequencies by the high electron drift velocity and reach the ion acoustic wave range. The instability occurs when the two modes merge [12]. The magnetic field and the electron drift velocity are the main sources of the $\mathbf{E} \times \mathbf{B}$ electron drift instability. Plasma density, temperature and magnetic field gradients as well as ion flows can also play a role [13]. This instability is observed in many magnetized plasma devices like magnetrons for material processing [14], magnetic filters [15], Penning gauges [16], linear magnetized plasma devices dedicated to study cross-field plasma instabilities [17], Hall thrusters [1] and many fusion devices.

The transport resulting directly from this instability has not been quantified yet and the mechanism of the instability-electron interaction in this case has not been

studied. This paper proposes a first investigation into those questions based on a simple model calculation. In particular, we study the electrons dynamics in a slowly time varying ($\omega \ll \omega_{ce}$) potential profile in the presence of a constant axial electric field and a radial magnetic field. The ion dynamics and their effect on electrons are not considered in this model, and in that sense in our model the system is not self-consistent.

The paper is organized as follows. In section II, we briefly describe the Hall thruster mechanism and the model considered for the wave dispersion relation and spectrum. In section III, the numerical scheme used for particle trajectory integration is detailed. In section IV, we study the behavior of an electron interacting with only one Fourier mode fulfilling the instability dispersion relation of the $\mathbf{E} \times \mathbf{B}$ electron drift instability. In section V, we study the behavior of an electron interacting with three Fourier modes. In section VI, we show that due to the strong wave-particle interactions, the dynamics of each electron becomes chaotic, and in the presence of more than one wave, we find a significant amount of cross-field electron transport along the axial direction.

II. ELEMENTARY MODEL

In a Hall thruster, plasma is formed between two co-axial dielectric cylinders. Electrons are injected from an emissive cathode placed outside the exhaust plane and, due to the presence of the strong radial magnetic field, these electrons start to gyrate around magnetic lines and become magnetized. The combination of the axial electric field and the radial magnetic field generates a strong $\mathbf{E} \times \mathbf{B}$ drift motion in the azimuthal direction. This creates closed Hall current loops. The magnetized electrons are trapped in this configuration and stay for a long time within the channel. This results in a decrease of the electron conductivity in the axial direction. Xenon atoms injected through the anode at the end of the channel are ionized by the electrons drifting at a high velocity. Since the ions are not magnetized, they are extracted from the plasma and the axial electric field accelerates them from the ionization region without collision, as sketched in Fig. 1. The electrons injected from an emissive cathode help to generate the plasma and also help to neutralize the ion beam. We consider a Cartesian coordinate system for the numerical modeling, with the x -direction as the magnetic field direction, the y -direction as the $\mathbf{E} \times \mathbf{B}$ drift direction and the z -direction as the constant electric field direction, representing the radial, azimuthal and axial directions respectively of the thruster chamber. Fig. 1 presents these three directions.

In the context of a Hall thruster, using a cold fluid equation for unmagnetized ions and a Vlasov kinetic equation for magnetized electrons, Cavalier *et al.* [10] derived a 3D dispersion relation for the $\mathbf{E} \times \mathbf{B}$ drift in-

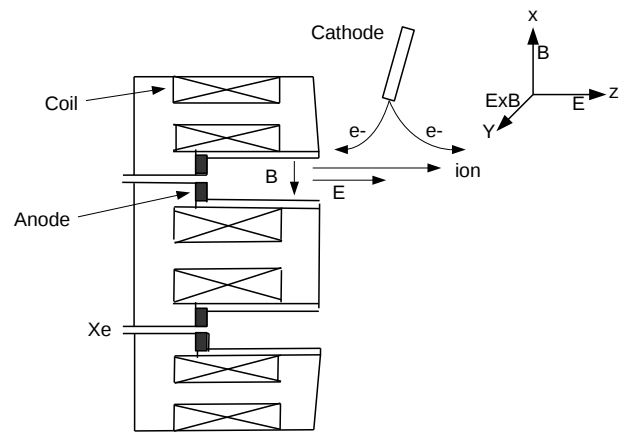


FIG. 1: Schematic diagram of Hall thruster. B is the magnetic field, E_0 is the constant axial electric field, e^- denotes electrons, and the top-right sketch presents the Cartesian coordinates for our numerical simulation.

stability in the form

$$1 + k^2 \lambda_{De}^2 + g \left(\frac{\omega - k_y v_d}{\omega_{ce}}, (k_x^2 + k_z^2) \rho_e^2, k_x^2 \rho_e^2 \right) - \frac{k^2 \lambda_{De}^2 \omega_{pi}^2}{(\omega - k_z v_{i,b})^2} = 0, \quad (1)$$

where λ_{De} is the electron Debye length, $v_d = E_z/B$ is the electron drift velocity, $v_{i,b}$ is the ion beam velocity, $\rho_e = v_{the}/\Omega_{ce}$ is the electron Larmor radius, v_{the} is the electron thermal velocity; ω , ω_{ce} and ω_{pi} are the mode, electron cyclotron and ion plasma frequency, respectively, while k_x , k_y , k_z and k are the x , y and z components and modulus of wave vector \mathbf{k} , respectively. g is the Gordeev function [18]: $g(\Omega, X, Y) = \frac{\omega}{2Y} \exp(-X) \sum_{m=0}^{\infty} Z(\frac{\Omega - m}{\sqrt{2Y}}) I_m(X)$ where $Z(x)$ is the plasma dispersion function and I_m is the modified Bessel function of first kind. This instability described by Eq. (1) can grow to a sufficient level of turbulence into a non-magnetic ion-acoustic instability with modified angular frequency and growth rate [7]

$$\begin{aligned} \omega &\approx k_x v_{i,b} + \frac{k c_s}{\sqrt{1 + k^2 \lambda_{De}^2}}, \\ \gamma &\approx \sqrt{\frac{\pi m_e}{8 m_i}} \frac{k_y v_d}{(1 + k^2 \lambda_{De}^2)^{3/2}}, \end{aligned} \quad (2)$$

respectively, where c_s is the ion acoustic velocity. This analytical model for the dispersion relation fits well with experimental data. We consider a constant electric field $\mathbf{E}_0 = E_0 \hat{e}_z$ along the z -direction and a constant magnetic field $\mathbf{B} = B_0 \hat{e}_x$ along x -direction.

Experimentally, the observed propagation angle of the instability-generated wave deviates by $\tan^{-1}(k_z/k_y) \sim 10 - 15^\circ$ from the azimuthal y -direction near the thruster exit plane. Further from the exit plane, the propagation becomes progressively more azimuthal [3]. Hence, the wave vector along the axial direction $k_z \sim 0.2 k_y$, and the

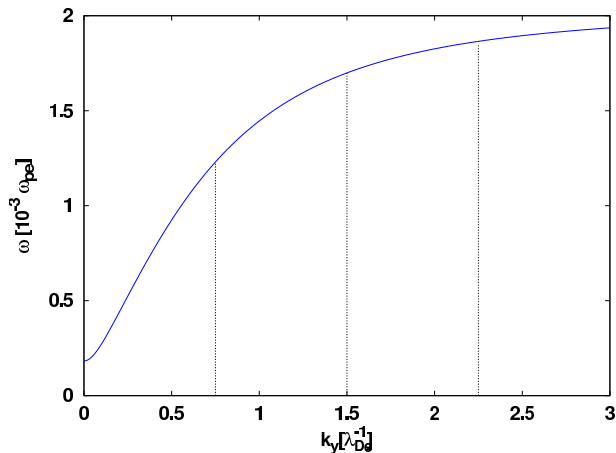


FIG. 2: Solutions of the 3D $\mathbf{E} \times \mathbf{B}$ electron drift instability for $k_x = 0.03$. The three vertical lines locate the three modes which are taken for our numerical study.

electric field along the axial direction is dominated by the stronger constant field $E_0 \hat{\mathbf{e}}_z$. Therefore for simplicity, we consider that the unstable modes are confined in $x - y$ (i.e., $r - \theta$) plane only. Then, the time varying part of the potential in $x - y$ plane is constructed as a sum of unstable modes. The total electric field acting on the particle is

$$\mathbf{E}(x, y, z, t) = \sum_n (k_{nx} \hat{\mathbf{e}}_x + k_{ny} \hat{\mathbf{e}}_y) \phi_{0n} \sin \alpha_n(x, y, t) + E_0 \hat{\mathbf{e}}_z, \quad (3)$$

with local phase $\alpha_n(x, y, t) = k_{nx}x + k_{ny}y - \omega_n t + \zeta_n$, where n is a label for different modes with wave vector \mathbf{k}_n , angular frequency ω_n and phase ζ_n . \mathbf{k}_n , ω_n follow the dispersion relation eq. (1) and phases ζ_n are random. Here, the position \mathbf{r} , velocity \mathbf{v} , time t , and potential ϕ_0 are normalized with Debye length λ_{De} , thermal velocity v_{the} , reciprocal ω_{pe}^{-1} of the electron plasma frequency, and $m_e v_{the}^2 / |q_e|$, respectively. We choose the amplitude ϕ_{0n} of all the modes equal to the saturation potential [7] at the exit plane of the thruster $|\delta\phi_{y,rms}| = T_e / (6\sqrt{2}) = 0.056 m_e v_{the}^2$.

We consider three modes ($n = 1, 2, 3$) with $(k_{nx}, k_{ny}, \omega_n) = (0.03, 0.75, 1.23 \times 10^{-3})$, $(0.03, 1.5, 1.7 \times 10^{-3})$ and $(0.03, 2.25, 1.87 \times 10^{-3})$, respectively. The location of these three modes is shown in Fig. 2 by three vertical lines. In normalized units, $|q_e|B_0/m_e = 0.1 \omega_{pe}$, $|q_e|E_0/m_e = 0.04 \omega_{pe} v_{the}$, and $v_d = 0.4 v_{the}$. Therefore, for all three modes, the y -component of phase velocity $\omega_n/k_{ny} \ll v_d$.

III. NUMERICAL METHOD

The equations of motion of the particle are

$$\frac{d\mathbf{r}}{dt} = \mathbf{v}, \quad \frac{d\mathbf{v}}{dt} = \frac{q_e}{m_e} (\mathbf{E} + \mathbf{v} \times \mathbf{B}). \quad (4)$$

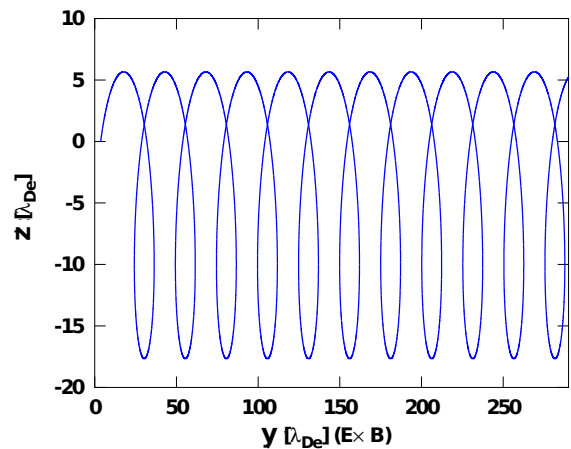


FIG. 3: Regular trajectory of a single particle in presence of a constant magnetic field $\omega_c = 0.1 \omega_{pe}$ and a constant electric field $E_0 = 0.04$.

Because \mathbf{E} depends on space, the infinitesimal generators for both equations do not commute, and one uses a time-splitting numerical integration scheme. The first equation is integrated in the form $\mathbf{r}(t + \Delta t) = \mathcal{T}_{v,\Delta t}(\mathbf{r}(t)) = \mathbf{r}(t) + \mathbf{v}\Delta t$. For the second equation, we separate the electric integration $\mathbf{v}(t + \Delta t) = \mathcal{T}_{E,\Delta t}(\mathbf{v}(t)) = \mathbf{v}(t) + (q_e/m_e)\mathbf{E}\Delta t$ from the magnetic integration, which solves only the gyro-motion. For the latter, we use the Boris method [19], formally $\mathbf{v}(t + \Delta t) = \mathcal{T}_{B,\Delta t}(\mathbf{v}(t))$. As a result, we use a second-order symmetric scheme

$$\begin{pmatrix} \mathbf{r}(t + \Delta t) \\ \mathbf{v}(t + \Delta t) \end{pmatrix} = \mathcal{A} \begin{pmatrix} \mathbf{r}(t) \\ \mathbf{v}(t) \end{pmatrix}, \quad (5)$$

with the nonlinear map

$$\mathcal{A} = \mathcal{T}_{v,\Delta t/2} \circ \mathcal{T}_{E,\Delta t/2} \circ \mathcal{T}_{B,\Delta t} \circ \mathcal{T}_{E,\Delta t/2} \circ \mathcal{T}_{v,\Delta t/2}. \quad (6)$$

To understand the effect of waves, we first solve the equations of motion Eq. (4) numerically for a single particle trajectory with initial velocity $v_{0x} = 0, v_{0y} = 1$ and $v_{0z} = 1$ in presence of a constant electric field $E_0 = 0.4$ along z -direction and a constant magnetic field along x -direction such that $\omega_c = 0.1 \omega_{pe}$. Since there is no background electrostatic wave ($E_x = E_y = 0$), the particle exhibits regular cycloid motion. Therefore, the position co-ordinates x, y, z follow the relation $(y - c - a\tau)^2 + (z - b)^2 = c^2 + b^2$, where $a = v_d/\omega_c$, $b = (v_d - v_{0y})/\omega_c$, $c = v_{0z}/\omega_c$ and $\tau = \omega_c t$ and the velocity components are $v_x = v_{0x}, v_y = v_{\perp 0} \cos(\tau) + v_d$ and $v_z = v_{\perp 0} \sin(\tau)$, where $v_{\perp 0} = \sqrt{v_{0z}^2 + (v_{0y} - v_d)^2}$ and (v_{0x}, v_{0y}, v_{0z}) are the initial velocity components. Figs 3 and 4 present the trajectory and the velocity components of the particle. Along the y -direction, there is a drift velocity $v_d = 0.4 v_{the}$. Since $v_x = 0$, the trajectory is confined in the $y - z$ plane.

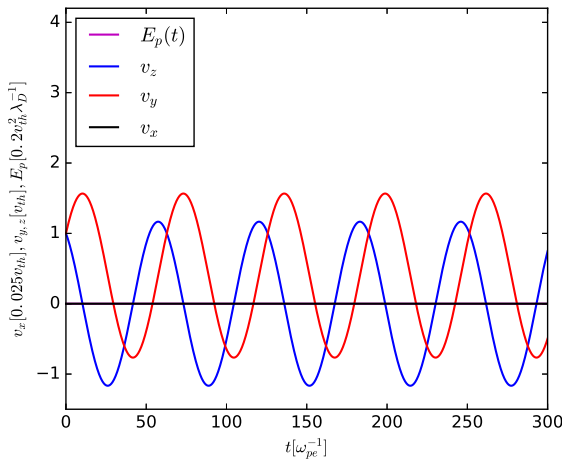


FIG. 4: Three components of velocity v_x (black), v_y (red), v_z (blue) and the y -component of electric field at the particle location $E_p(t)$ (magenta). Since there is no background electrostatic wave, the electric field amplitude at the particle location vanishes and the magenta line coincides with the black one.

IV. PARTICLE TRAJECTORY IN PRESENCE OF ONE WAVE

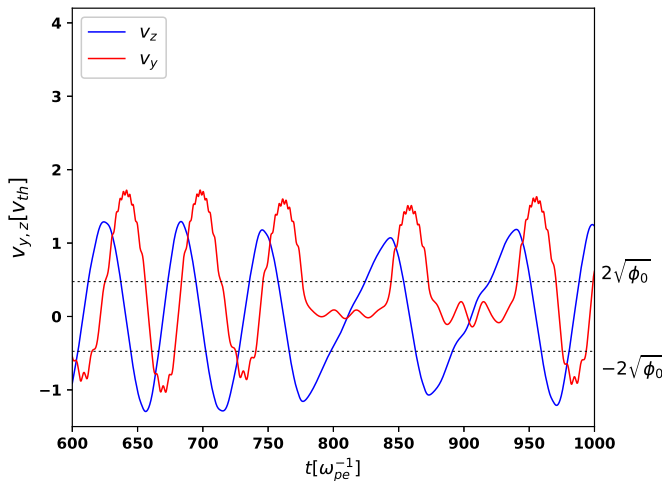


FIG. 5: Particle evolution in the presence of a single background electrostatic wave with $n = 2$. Velocity components v_y (red) and v_z (blue) of one particle. Near $t = 800$ and 900 , the particle is trapped in the wave potential and it oscillates with the time period $\tau_b = 18\omega_{pe}^{-1}$.

In the presence of a background electrostatic wave, the wave-particle interaction modifies the cyclotron motion. The strength of the wave-particle interaction depends on the wave amplitude and the particle velocity. Fig. 5 presents the time evolution of v_y (red line) and v_z (blue line), and Fig. 6 presents the time evolution of v_x (black line) and the y -component $E_p(t)$ of electric field at particle location (magenta line). Due to the cyclotron motion, v_y oscillates about the drift velocity $v_d = 0.4$. During

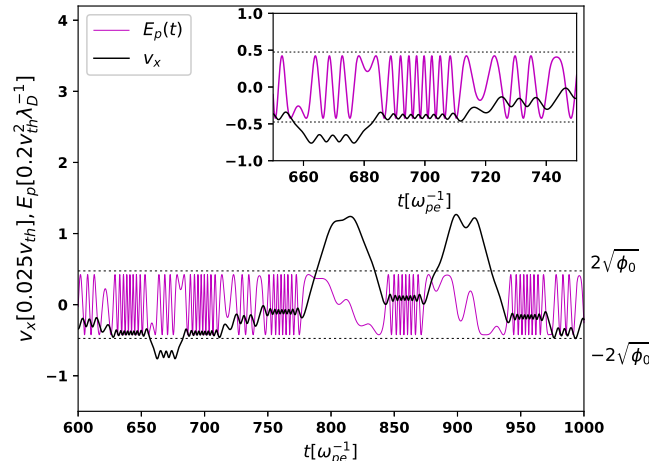


FIG. 6: Particle evolution in the presence of a single background electrostatic wave with $n = 2$. v_x (black solid line), electric field at particle location $E_p(t)$ (magenta line). Black dotted horizontal lines show the location of $\pm 2\sqrt{\phi_0}$.

each cyclotron oscillation, when $|v_y| \leq 2\sqrt{\phi_0}$ (denoted by black dashed lines) the particle interacts strongly with the electrostatic wave, and the electric field $E_p(t)$ enhances/reduces the v_x value by a large amount.

The inset of Fig. 6 presents, during a strong interaction, according to the sign of E_p , jumps of v_x in positive and negative direction. Moreover, during this strong interaction depending on the local potential profile, the particle may be trapped in the wave potential well and oscillate with the bounce frequency $\omega_b = 0.35\omega_{pe}$. In Fig. 5 near $t = 800$ and 900 , it is trapped. One essential condition for the trapping is $\omega_b > \omega_c$, where $\omega_b = k_y \sqrt{|q_e| \phi_0 / m_e}$ is the bounce frequency. Since $k_y \gg k_x$, the condition for trapping is easily satisfied along the y -direction, therefore the particle bounces back and forth along the y -direction and moves freely along the x -direction. Hence, along the x -direction it gains/loses energy from/to the wave, which causes a large change in v_x . Finally, depending on the local potential value, it may escape from the wave and again start to exhibit cyclotron motion. Therefore, the duration of trapping depends on v_x and ω_b/ω_c . It is observed that, for small $v_x \ll \sqrt{\phi_0}$, this trapping is easily observed for $\omega_b/\omega_c \geq 2$.

Outside the strong interaction region, due to the large particle velocity, the electric field at particle location E_p changes rapidly, which generates the small-amplitude fast oscillation in v_x . The component v_y is also modulated due to this fast change in $E_p(t)$. Since the electric field along z -direction $E_0 \hat{e}_z$ is constant, the amplitude of the fast oscillation in v_z is negligible. The motion along the z -direction is coupled with the other two directions due to $\mathbf{v} \times \mathbf{B}$ term of Lorentz force, therefore v_z is also modified during the strong interactions. In Fig. 5 at $t = 900$, during trapping, the oscillation of v_z is observed with

frequency ω_b , on top of cyclotron motion.

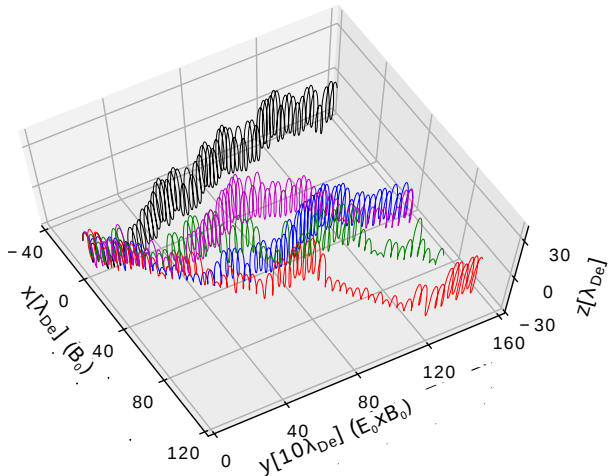


FIG. 7: Trajectories of 5 different particles with different initial phase in the presence of a single background electrostatic wave with $n = 2$.

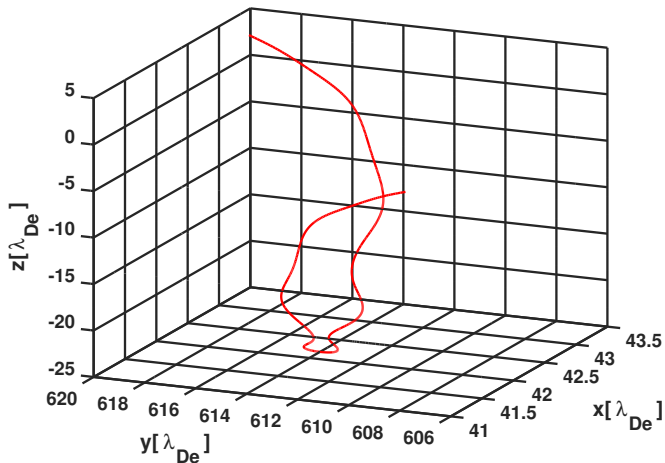


FIG. 8: Trajectory of single particle during trapping.

Fig. 7 displays the trajectories of 5 particles with slightly different initial positions. In the absence of the electrostatic wave, they exhibit cyclotron motion with drifting guiding center, and their trajectories remain confined in the $y-z$ plane. Due to the strong interaction with the electrostatic wave in presence of magnetic field, each trajectory evolves differently and they separate exponentially from each other, so that the dynamics becomes chaotic. Each strong interaction causes a change in the trajectories along x , and, depending on the strength of the electric field at particle location, v_y may increase or decrease after each strong interaction, which modifies the gyroradius ($r_b = v_\perp/\omega_c$) accordingly.

Fig. 8 presents a small portion of trajectory during trapping. Since the particle is trapped along y -direction,

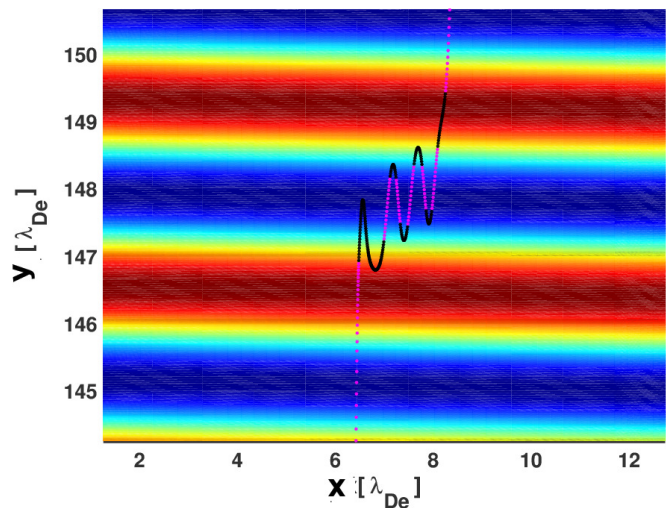


FIG. 9: Trapping of particle in the potential well of background wave. Magenta dots: particle energy higher than the maximum potential energy ϕ_0 of the background wave. Black dots: particle energy below ϕ_0 . The colour surface plot presents the potential profile of the background wave where red denotes the larger values and blue the lower values.

it oscillates within the wavelength $\lambda = 2\pi/k_y \sim 4\lambda_{De}$ and Fig. 9 presents the $x-y$ projection of the trajectory during trapping. The colour surface plot presents the background wave potential. Since $\omega \ll \omega_c$, during the strong interaction the wave potential remains constant. The magenta dots mark the particle location when its energy is greater than the maximum potential energy of the electrostatic wave ϕ_0 , and black dots are associated with the particle energy below ϕ_0 . During climbing up the potential hill, it loses energy and oppositely it gains energy during descent; finally, if, at the top of the potential hill (dark red), the particle energy is greater than the potential energy ϕ_0 , it detrap from the potential well. Therefore, the trapping phenomena depend on the wave potential at the particle location: sometimes it may get trapped in the potential well and sometimes it just takes energy from the wave and escapes from the potential well. During trapping, its average y location remains unchanged. Due to this strong wave-particle interaction, the dynamics of the particle becomes chaotic. The duration of strong interaction depends on ω_b/ω_c , therefore, for a single wave, chaos will occur for amplitudes ϕ_0 satisfying the inequality $\phi_0 \geq \omega_c^2/k_y^2$. For thruster parameter values, all three waves individually satisfy this criterion.

In the presence of two and three waves, the dynamics becomes more chaotic and this threshold value is reduced. With increase of the potential ϕ_0 and the wave vector k_y , the bounce frequency of the particle increases, which makes the dynamics more chaotic and particles are trapped more frequently in the electrostatic wave.

V. INTERACTIONS WITH THREE WAVES: ENERGY GAIN AND AXIAL TRANSPORT

To analyze the transport, we consider 1056 particles with random initial positions in the rectangle $0 \leq x_0 \leq 2\pi/k_{1x}$, $0 \leq y_0 \leq 4\pi/k_{1y}$, $z_0 = 0$ and with velocities drawn from a 3D Gaussian distribution with unit standard-deviation (viz. the thermal velocity) along all three directions. Then we evolve their dynamics in the presence of all three waves with equal amplitude $\phi_{n0} = \phi_{0,\text{rms}}$. For single wave interaction, the Hamiltonian of the dynamics can be written in a time independent form and therefore, though the dynamics remains chaotic, there is no net gain/loss of energy over long time evolution. Hence, due to the chaotic dynamics, in presence of the single wave, we get a very small amount of cross-field transport along the z direction, but the diffusion coefficient is very small.

But in presence of two or more waves, the Hamiltonian is no longer time independent, all the trajectories become chaotic and, due to the wave-particle interaction, they gain energy from the waves. The particles net perpendicular velocity components v_y, v_z increase. After a sufficiently long time-evolution, they form a Gaussian-like velocity distribution profile with higher temperature along y - and z -directions. Since $E_x \ll E_{y,z}$, the increase of the velocity component along the magnetic field is negligible compared to the other two directions. Therefore, the temperature along the magnetic field remains nearly unchanged. Fig. 10 presents the initial ($t = 0$) (solid yellow bars) and final ($t = 5 \times 10^4 \omega_c^{-1}$) (bars with red border) velocity distribution of v_z , which presents a significant increase of temperature along perpendicular direction T_\perp compared to the parallel direction, $T_\perp/T_\parallel \sim 4$.

In the thruster chamber, there is an insulating boundary along x -direction. The width of the annular space in the thruster is $240 \lambda_{De}$. Therefore the particles are reflected when they reach the boundary. If there

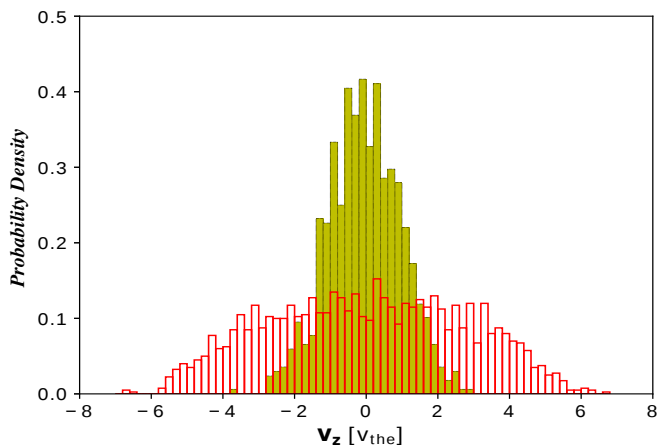


FIG. 10: Velocity distribution along z at $t = 0$ (yellow solid bar) and at $t = 5 \times 10^4 \omega_{pe}^{-1}$ (bar with red boundary).

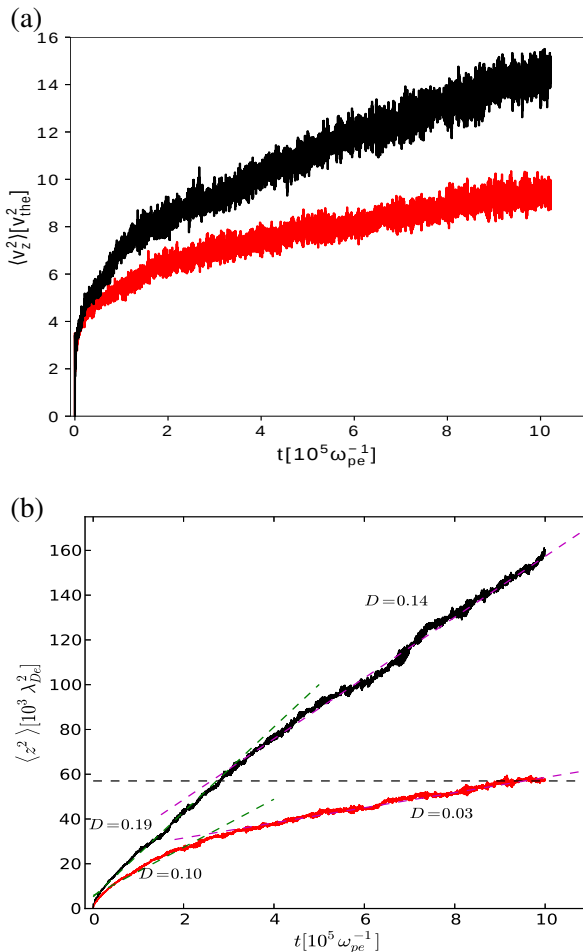


FIG. 11: Panels (a) and (b): mean square velocity dispersion $\langle v_z^2(t) \rangle$ and mean square displacement $\langle z^2(t) \rangle$, respectively. The red and black lines correspond to no-boundary and reflecting boundary cases, respectively. Panel (b) reveals two diffusion regimes in each curve, namely slopes (0.10, 0.03) for no-boundary and (0.18, 0.14) for reflecting boundary.

were no reflection, particles would proceed under the same dynamics (red line in Fig. 11(a)-(b)). To account for reflection (black line), we consider the Debye sheath electron potential energy near the wall [20] to be $\phi_{sh} = 20 \text{ eV} = 0.8 m_e v_{the}^2$. Electrons reaching the wall with $v_x < \sqrt{0.8}$ are specularly reflected, and electrons with $v_x > \sqrt{0.8}$ are isotropically reflected from the wall while conserving their total energy.

Fig. 11(a)-(b) present $\langle v_z^2(t) \rangle$ and $\langle z^2(t) \rangle$ for reflecting boundary (black) and without boundary (red), where $\langle \cdot \rangle$ denotes the average over number of particles for the deviation from the ballistic motion. Thus, $\langle z^2 \rangle := \langle (z(t) - v_{z0}t)^2 \rangle$, $\langle v_y \rangle := \langle (v_y(t) - v_{y0}) \rangle$, $\langle v_z \rangle := \langle (v_z(t) - v_{z0}) \rangle$ and $\langle v_z^2 \rangle := \langle (v_z(t) - v_{z0})^2 \rangle$. The duration of strong interaction with the waves and hence the gain of energy from the waves decrease for larger particle velocity. Therefore, the rate of energy gain in Fig. 11(a) decreases with time

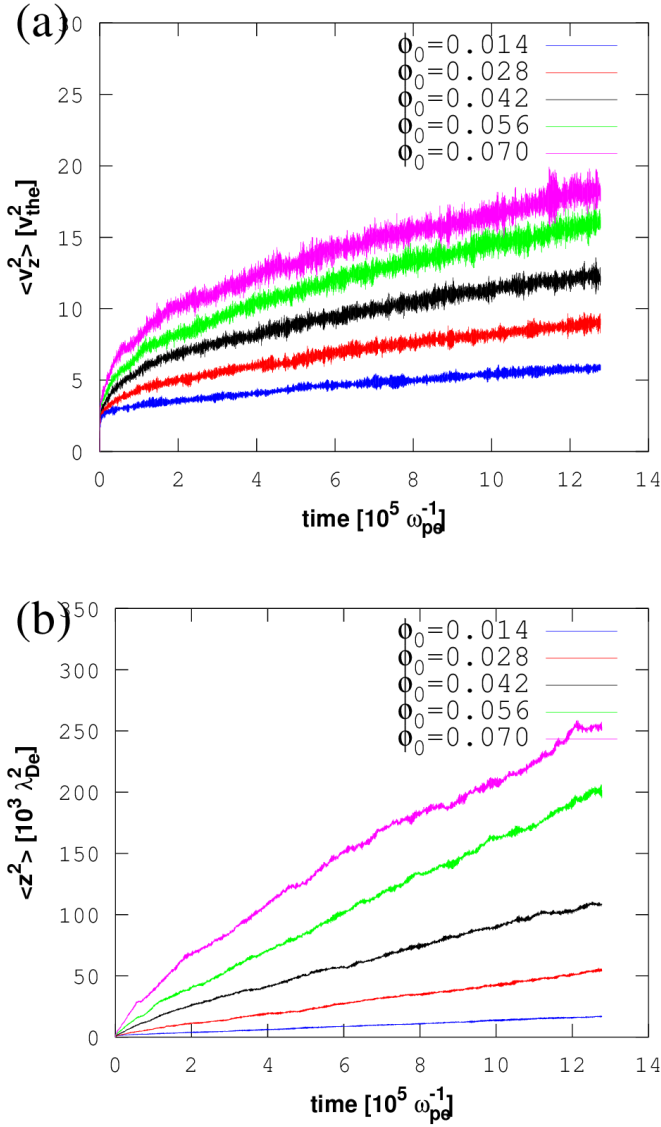


FIG. 12: Panel (a): $\langle v_z^2 \rangle$ evolution for different amplitude of the waves. Panel (b): $\langle z^2 \rangle$ evolution for different wave amplitudes.

for both cases.

In isotropic reflection, the velocity components of the particle are redistributed randomly in three directions, a particle with small v_y and v_x gains more energy from the electrostatic wave compared to that having higher v_y and v_x . Therefore, in presence of reflecting boundary, particles gain more energy than in absence of reflection. The dashed black line marks the location of thruster outlet along the z -direction. Since with reflection they gain more energy, their mean square displacement along z -direction crosses the thruster outlet, and they exit from the thruster chamber more quickly than in the case without boundary. For both cases, we found two different regimes of transport. Although the particle motion is not brownian, one may define an effective diffusion coefficient $D = d\langle z^2 \rangle / dt$ in the direction of the

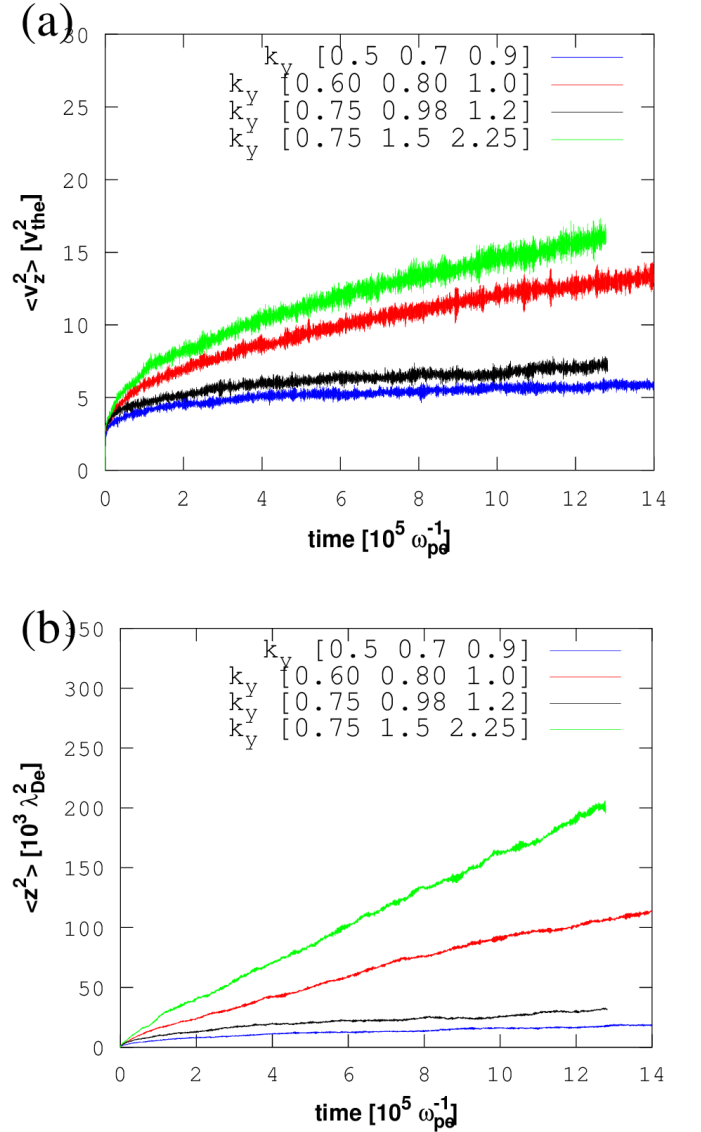


FIG. 13: Panel (a): $\langle v_z^2 \rangle$ evolution for different k_y values of the waves. Panel (b): $\langle z^2 \rangle$ evolution for different k_y values waves.

static electric field \mathbf{E}_0 , as the average of the slope of $\langle z^2 \rangle$ as a function of time. While the derivative $d\langle z^2 \rangle / dt$ is fluctuating strongly, the trend is quite stable over time spans on the order of $10^5 \omega_{pe}^{-1}$. Its observed values are $D = (0.1, 0.03)$ for no-reflection and $D = (0.18, 0.14)$ for reflecting boundary. The change in slope around $t = 2 \times 10^5 \omega_{pe}^{-1}$ is related to the different structure formation of the stochastic web, controlling the velocity transport [21, 22].

The cross-field transport and the energy gain by the particles depend on the duration of wave-particle interaction determined by the ratio ω_b / ω_c . Since $\omega_b \propto \sqrt{\phi_0}$, the cross-field transport and the energy gain from the wave will be higher for higher amplitude of the background waves. Figs 12(a) and (b) present the time evolution of $\langle v_z^2 \rangle$ and $\langle z^2 \rangle$ for five different amplitudes of the waves

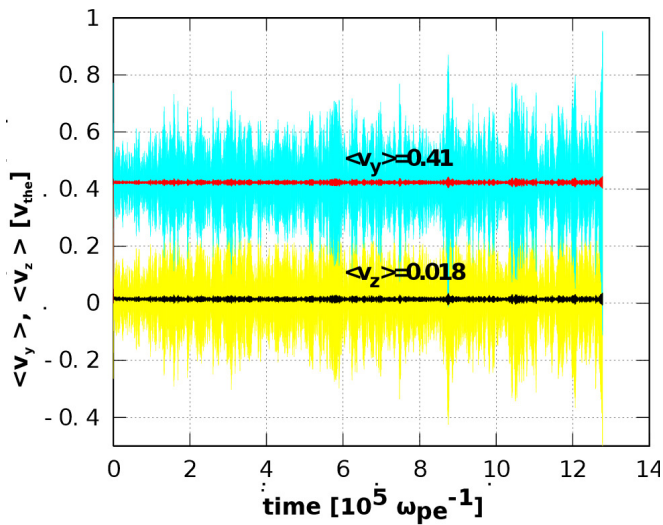


FIG. 14: Time evolution of $\langle v_y \rangle$ (cyan) and $\langle v_z \rangle$ (yellow) of 1056 particles. The solid red line and the black line present the time average of the $\langle v_y \rangle$ and $\langle v_z \rangle$.

$\phi_0 = 0.014, 0.028, 0.042, 0.056$ and 0.070 .

Moreover, the strength of the electric field and the bounce frequency ω_b are proportional to the wave number k_y , therefore $\langle v_z^2 \rangle$ and $\langle z^2 \rangle$ increase for larger k_y of the three waves. Fig. 13(a) and (b) present $\langle v_z^2 \rangle$ and $\langle z^2 \rangle$ for four different sets of k_y values, $(k_{y1}, k_{y2}, k_{y3}) = (0.5, 0.7, 0.9); (0.6, 0.8, 1); (0.75, 0.98, 1.2); (0.75, 1.5, 2.25)$. For the 2nd and 4th cases, the k_y values are the harmonics of $k_y = 0.2$ and 0.75 , respectively. The large values of $\langle v_z^2 \rangle$ and $\langle z^2 \rangle$ for these two cases are due to the formation of stochastic webs, which help in long range transport [23]. For the other two cases where the k_y values are not harmonics, there is no stochastic web formation, so that $\langle v_z^2 \rangle$ and $\langle z^2 \rangle$ are small for those two cases.

In Hall thrusters, it is experimentally observed [2] that the ratio of azimuthal to axial current-density $J_y/J_z \sim 10$. In our numerical study, we use 1056 particles with random initial positions in the rectangle $0 \leq x_0 \leq 2\pi/k_{1x}$, $0 \leq y_0 \leq 4\pi/k_{1y}$, $z_0 = 0$ and with velocities drawn from a 3D Gaussian distribution with unit standard-deviation along all three directions. We observe that the velocity distributions along z - and y -directions are nearly identical, therefore the number densities along these two directions are equal. We can compare the mean velocity ratio with the mean current density ratio along these two directions. Fig. 14 shows that $\langle v_y \rangle = 0.41$ and $\langle v_z \rangle = 0.018$, so that $\langle v_y \rangle / \langle v_z \rangle \sim 20$, which is of the same

order as the experimental observation.

VI. CONCLUSIONS

In this paper, we carried out model calculations to provide a dynamical basis for the high value of the experimentally observed anomalous cross-field transport in thruster configurations. The underlying mechanism is associated with the chaotic dynamics of electrons due to their interaction with a spectrum of unstable electrostatic waves. The electrostatic waves are generated due to the $\mathbf{E} \times \mathbf{B}$ electron drift instability. In the presence of a magnetic field B_0 , an axial constant electric field E_0 and the electrostatic waves, the drifted cyclotron motion becomes chaotic due to the strong wave-particle interaction. In presence of more than one wave, the electrons gain energy over long time evolution and their temperature is increased along the perpendicular direction. This chaotic dynamics helps in the transport of electrons along the thruster axial direction.

A significant amount of axial electron transport is observed in presence of more than one wave, and the electrons exit from the thruster chamber. The reflection at boundary enhances the transport coefficient. The duration of wave-particle interaction depends on the ratio ω_b/ω_c of bounce frequency to cyclotron frequency. With increase of amplitude and k_y values of the background waves, the value of the bounce frequency increases, which enhances the energy exchange rate and the anomalous diffusion coefficient. The existence of harmonics in k_y helps to generate different stochastic webs, which increases the diffusion coefficient. The average velocity ratio along azimuthal to axial direction $\langle v_y \rangle / \langle v_z \rangle$ in our numerical model is in good agreement with experimental observations.

Acknowledgements

We acknowledge the financial support from CE-FIPRA/IFCPRA through project 5204-3. This work was granted access to the HPC resources of Aix-Marseille Université [24] financed by the project Equip@Meso (ANR-10-EQPX-29-01) of the program Investissements d'Avenir supervised by the Agence Nationale de la Recherche. We are grateful to Professors Xavier Leoncini, Dominique Escande and Abhijit Sen for many fruitful discussions and their comments.

- [1] A. I. Morozov and V. V. Savelyev, Rev. Plasma Phys. **21**, 203 (2000).
 [2] G. S. Janes and R. S. Lowder, Phys. Fluids **9**, 1115 (1966).

- [3] S. Tsikata, C. Honoré, N. Lemoine, D. M. Grésillon, Phys. Plasmas **17**, 112110 (2010).
 [4] A. Smirnov, Y. Raitses and N. J. Fisch, Phys. Plasmas **14**, 057106 (2007).

- [5] J. C. Adam, A. Héron, and G. Laval, *Phys. Plasmas* **11**, 295 (2004).
- [6] T. Lafleur, S. D. Baalrud and P. Chabert, *Phys. Plasmas* **23**, 053502 (2016).
- [7] J. P. Boeuf and L. Garrigues, *Phys. Plasmas* **25**, 061204 (2018).
- [8] N. A. Marusov, E. A. Sorokina, V. P. Lakhin, V. I. Ilgisonis and A. I. Smolyakov, *Plasma Sources Sci. Tech.* **28**, 015002 (2019).
- [9] J. C. Adam, J. P. Boeuf *et al.*, *Plasma Phys. Control. Fusion* **50**, 124041 (2008).
- [10] J. Cavalier, N. Lemoine, G. Bonhomme, S. Tsikata, C. Honoré and D. Grésillon, *Phys. Plasmas* **20**, 082107 (2013).
- [11] P. S. Gary, *J. Plasma Phys.* **6**, 561 (1971).
- [12] P. S. Gary and J.J. Sanderson, *J. Plasma Phys.* **4**, 739 (1970).
- [13] A. B. Mikhailovskii, *Electromagnetic instabilities in an inhomogeneous plasma*, transl. E. W. Laing, Institute of Physics Publishing (Bristol, 1992).
- [14] S. N. Abolmasov, *Plasma Sources Sci. Technol.* **21**, 035006 (2012).
- [15] J. P. Boeuf, J. Claustre, B. Chaudhury and G. Fubiani, *Phys. Plasmas* **19**, 113510 (2012).
- [16] C. L. Ellison, Y. Raitses and N. J. Fisch, *Phys. Plasmas* **19**, 013503 (2012).
- [17] M. Matsukuma, Th. Pierre, A. Escarguel, D. Guyomarc'h, G. Leclert, F. Brochard, E. Gravier and Y. Kawai, *Phys. Lett. A* **314**, 163 (2003).
- [18] G. V. Gordeev, *Zh. Eksp. Teor. Fiz.* **23**, 660 (1952) [*Sov. Phys. JETP* **6**, 660 (1952)].
- [19] J. Boris, *Proc. Fourth Conf. Numer. Simul. Plasmas*, NRL, Washington, D.C., pp. 3-67 (1970).
- [20] Yu Daren, Li Hong and Wu Zhiwen *Phys. Plasmas* **14**, 064505 (2007).
- [21] G. M. Zaslavsky, *Chaos* **1**, 1 (1991).
- [22] X. Leoncini, C. Chandre and O. Ourrad, *C. R. Mécanique* **336**, 530 (2008).
- [23] A. A. Vasil'ev and G. M. Zaslavskii, *Sov. Phys. JETP* **72**(5), 826 (1991).
- [24] *MesoCentre, Aix-Marseille Université* [<https://mesocentre.univ-amu.fr/en/>].